Acoustic response of an injection system to high-frequency transverse acoustic fields

A. Ficuciello, F. Baillot, J. Blaisot, C. Richard, Marie Théron

Special Issue – TIGRE

International journal of spray and combustion dynamics

International Journal of Spray and Combustion Dynamics
0(0) 1–13

DOI: 10.1177/1756827717735300
journals.sagepub.com/home/scd

SAGE

Acoustic response of an injection system to high-frequency transverse acoustic fields

A Ficuciello[1,2], F Baillot[1], JB Blaisot[1], C Richard[3] and M Théron[2]

Abstract

The acoustic coupling between the injection system and the acoustic fluctuations in liquid rocket engine combustion chambers is an important issue in the understanding of the thermo-acoustic instability phenomenon. This paper presents the results of a wide-ranging parametric investigation of the acoustic response of a two-phase injection system submitted to a forced high-amplitude transverse acoustic field. Two domes, one for the gas and one for the liquid, were expressly designed to feed three identical coaxial injectors. The internal mode shapes of the domes were characterized by measuring pressure signals at different locations in the domes. Experimental mode shapes showed good agreement with those predicted by numerical simulations. Acoustic pressure amplitudes up to 23% of those induced in the main cavity can be found in both the gas and liquid domes. The response efficiency in a dome depends on the position of the injectors' exit in the acoustic field.

Keywords

Acoustic coupling, coaxial injector, transverse mode, liquid rocket engines, thermo-acoustic instability

Date received: 29 September 2016; accepted: 11 September 2017

1. Introduction

The development of liquid rocket engine propulsion systems has historically been plagued by the phenomenon of combustion instabilities.[1,2] Several programs have been devoted to the investigation of this problem and both full-scale and sub-scale tests have been performed.[3,4] Hot fire tests indicate that among the different types of combustion instabilities, high-frequency transverse instabilities are considered as the most harmful for liquid rocket engine operations.

Although many years of research have been dedicated to solving the problem, there is still a lack of knowledge. The main problem comes from the numerous processes and sub-processes involved, as well as from the complexity of their potential interactions. Combustion in liquid rocket engines is never perfectly steady and fluctuations of pressure, temperature, and velocity are always present. Since the sub-processes that occur in between the injection and the chemical reactions are dependent on the combustion chamber pressure and aerodynamics, a feedback mechanism able to amplify the natural acoustic modes in a combustion chamber is often encountered.[5,6] The feedback mechanisms are commonly sub-classified into intrinsic and injection-coupled mechanisms.[1,6] The intrinsic mechanism implies that only the processes taking place after the propellant injection are responsible for the pressure fluctuation amplification in the chamber. The influence of these processes on liquid rocket engine combustion instability has been largely investigated in the literature[1,7,8] by treating sub-scale combustors, in lab-scale devices in sub-critical and super-critical conditions and by considering reacting[9–11] and non-reacting flows.[12,13] In the injection-coupled mechanism, the acoustic fluctuations in the combustion chamber interact with the natural frequencies of the injection

[1]Normandie Univ, UNIROUEN, INSA Rouen, CNRS, CORIA, Rouen, France
[2]CNES Launchers Directorate, Paris, France
[3]LMRS, UMR 6085, CNRS-Université de ROUEN, Saint Etienne du Rouvray, France

Corresponding author:
A Ficuciello, UMR 6614 – CNES Launchers Directorate, CORIA, Paris, France.
Email: ficuciea@coria.fr

system, causing flow-rate fluctuations which contribute significantly to the acoustic pressure amplification. It is thus clear that the design of the injection system, in particular that of the injectors, represents a key element for the stability of rocket engines. In 1969, Heidmann and Groeneweg[14] identified the injection-chamber acoustic coupling as a driving mechanism for high-frequency instabilities and demonstrated that pressure fluctuations may be suppressed through appropriate acoustic design of the manifold. Research activities on the Common Research Combustor at the German Aerospace Center (DLR) highlighted the importance of the characterization of the acoustic modes of the injection system/chamber, in the interpretation of experimental results,[15–17] and a numerical study on the same experimental set-up also highlighted the impact of coupled acoustic cavities on resonance frequencies.[18] Injection-chamber coupling phenomenon has been also treated by Hardi et al.[19–21] The use of an acoustic baffle in the hydrogen manifold was necessary in that case to reduce acoustic coupling. The impact of acoustic coupling between the injection system and combustion chamber in an another DLR sub-scale model combustor has been recently investigated by Urbano et al.[22] who used high-performance large-eddy simulation in combination with computational acoustics to simulate combustion instabilities in this combustor. By triggering instabilities in the chamber, they were able to obtain limit cycles and acoustic activity in the injection domes that successfully compared with experiments.

This paper focuses on the interaction between the injection system acoustics and acoustic transverse fluctuations forced in the main chamber. The injection system is composed of three coaxial injectors and two injection domes, one for the gas and one for the liquid. The acoustic field is forced in a semi-open resonant cavity by four compression drivers. A parametric investigation is performed in order to characterize the sensitivity of the injection system to some of its key geometrical features.

It will be shown that the response of the injection system is strongly affected by the position of the injectors along the acoustic axis, by the size of the domes, and by the dimensions of the connections between domes and injectors. Some of the experimental results are compared with numerical simulations performed with COMSOL Multiphysics® Software. The software was also used in the design process of the two injection domes. Some key aspects of the design procedure are discussed hereafter.

2. Experimental set-up

The experimental set-up, presented in Figure 1, is composed of an acoustic semi-open resonant cavity with

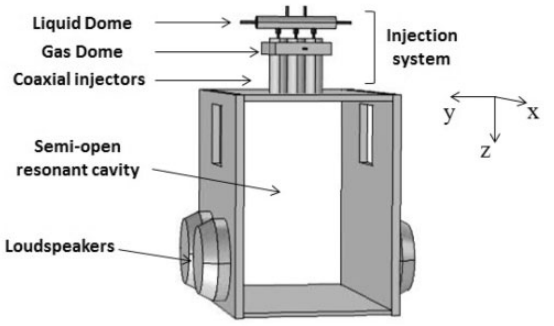

Figure 1. Schematic representation of the experimental set-up: main resonant cavity with two injection domes.

two parallel and vertical steel plates, a roof and a floor, both made of polyvinyl chloride. A pair of Beyma CP850Nd compression drivers is placed on each vertical plate to excite the second transverse mode of the cavity. The resulting acoustic field is characterized by a pressure anti-node (PAN) in the center of the cavity, two velocity anti-nodes (VANs), and four intensity anti-nodes (IANs). IAN is defined as the location where the product of the acoustic pressure and velocity fluctuations is maximum in the cavity. In the reference frame, $\vec{x}$ is the horizontal direction parallel to the cavity walls; $\vec{y}$ is the direction perpendicular to the walls and aligned with the acoustic axis, a.a.; and $\vec{z}$ is the vertical descending direction. Acoustic pressure peak-to-peak amplitudes up to 12,000 Pa are reached in the cavity at a frequency of 1 kHz.

This experimental set-up was previously used to characterize the influence of the acoustic field on the atomization process by using one to three identical coaxial liquid/gas injectors, fed by independent lines.[23–26] Water and air were used as working fluids. Injectors' geometries considered here are representative of actual liquid rocket engine devices.

Here, the injection system has been modified by implementing two injection domes (one for the gas and one for the liquid), in order to link the three injectors. The entire system is conceived in such a way that a large number of design parameters can be modified to investigate their influence on the acoustic coupling. In addition to these geometrical parameters, the injection conditions and the position of the injection system along the acoustic axis are also considered. The injection system assembly is shown in Figure 2 along with the main cavity. Three different configurations are shown:

- IAN-PAN-IAN: The central injector's exit is placed at the PAN and the two lateral ones at two IANs. The three injectors' exits are submitted to in-phase cavity pressure fluctuations symmetrically distributed relatively to the central plane (PAN);

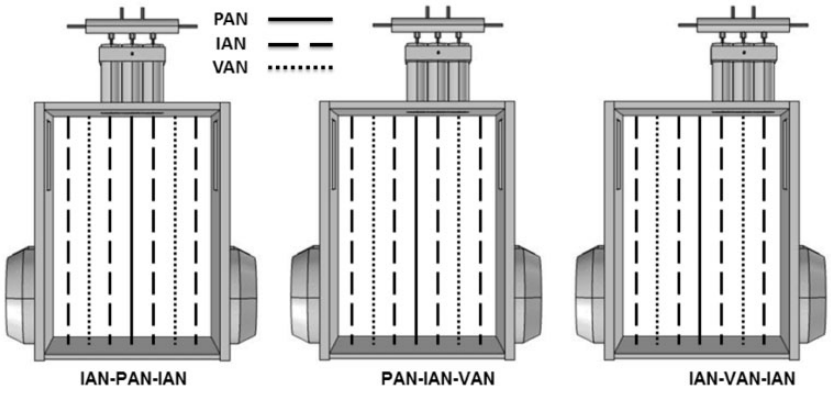

Figure 2. Scheme of the injection system placed on the main cavity roof according to three test configurations.

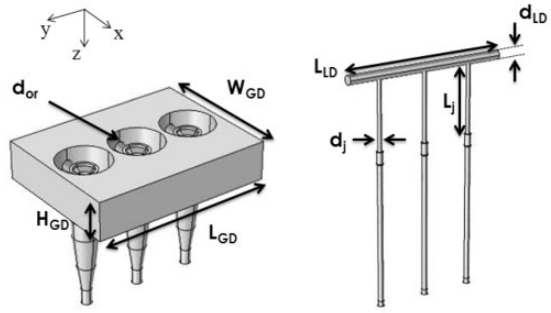

Figure 3. Gas dome, *GD*, (left side) and liquid dome, *LD*, (right side) internal domains considered in the numerical simulations.

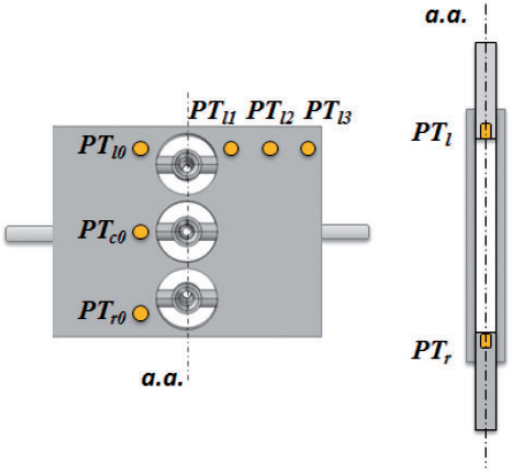

Figure 4. Schematic representation of pressure transducer locations in the gas dome (left side) and in the liquid dome (right side). Pressure transducers are represented in yellow.

- PAN-IAN-VAN: The three injectors' exits are submitted to different excitation conditions: VAN, IAN, and PAN, respectively. Acoustic pressure fluctuations in between VAN and PAN are in-phase and the amplitude decreases from PAN to VAN;
- IAN-VAN-IAN: The central injector's exit is placed at the VAN and the two lateral ones at two IANs, oscillating out-of-phase (non-symmetric excitation conditions).

Details of the gas and liquid domes are given in Figure 3. Pressure signals are recorded at different locations in the two injection domes. Up to four pressure transducers (PCB 106B) can be placed on the gas dome at the same time in order to characterize its acoustic response (see Figure 4). The liquid dome is provided with two pressure transducers PCB 113B28, which are flush-mounted inside the pistons as shown in Figure 4. A reference pressure is also measured in the main cavity at PAN.

A total of 180 test configurations were investigated to characterize the acoustic response of the gas dome, combining:

- five dome sizes indicated as *GD*0, *GD*2, *GD*4, *GD*6, and *GD*8, with *GD*0 representing the smallest dome volume and *GD*8 the largest. The dome sizes scale linearly with their indexes;
- three injector connection diameters (scaled with the outer injector's exit diameter): $d_{or} = 0.375$, $d_{or} = 0.75$, and $d_{or} = 1.125$;
- four air mass flow rates (scaled with the biggest mass flow rate): $\tilde{m}_{air} = 0$, $\tilde{m}_{air} = 0.4$, $\tilde{m}_{air} = 0.7$, and $\tilde{m}_{air} = 1$; and
- three spatial configurations of the injection system with respect to the acoustic axis (see Figure 2).

The maximum mass flow rate considered here ($\tilde{m}_{air} = 1$) corresponds to a Weber number $We_g = \rho_g U_g^2 D_l/\sigma = 400$. ρ_g and U_g are respectively the density and velocity of the air, D_l is the liquid post diameter, and σ is the water surface tension.

For the investigation of the liquid dome acoustic response, 60 test cases have been performed, combining:

- five dome sizes noted as *LD*0, *LD*05, *LD*1, *LD*15, and *LD*2, with *LD*0 representing the smallest dome volume and *LD*2 the largest;
- two injector connection lengths (scaled with the injector length): $L_j = 0.387$ and $L_j = 0.548$;
- two injector connection diameters (scaled with the injector's exit diameter): $d_j = 0.67$ and $d_j = 1$; and
- three spatial configurations of the injection system with respect to the acoustic axis (see Figure 2).

The liquid is injected at a Reynolds number $Re_l = D_l U_l/\nu_l = 2000$. U_l and ν_l are the liquid velocity and the kinematic viscosity, respectively.

The ability to change the size of the two domes, the kind of connections, and the position of the injection system along the acoustic axis provides a unique capacity for testing several resonant and coupling conditions with the same test bench.

The entire set-up is placed in an acoustically isolated room. A LabVIEW interface and an NI cDAQ module are used to manage the experiments. Dedicated software has been developed to automate generation and acquisition of the acoustic signals and to synchronize image acquisition when needed.

3. Dome characteristics

The two injection domes have been designed by taking into account the geometry of the three injector bodies that were already available. This fixed some constraints in terms of the domes' geometry. Domes' eigenmodes identification has been carried out with the *Acoustics* optional package of the finite element solver of COMSOL Multiphysics®. Simulations were performed with the *pressure acoustics* module in which the Helmholtz equation is solved in the frequency domain without source terms. Acoustic pressure is the only variable of the problem. The numerical parametric analysis determined the geometry (size, shape...) for the two injection domes. Figure 3 shows the final internal domains of the two domes considered in the simulations. These geometries have been used to calculate the domes' eigenmodes. The boundary conditions imposed at the injectors' exit plane are those of an open boundary ($p = 0$) while all other surfaces are treated as rigid walls (i.e., zero normal acoustic-velocity fluctuations); no mass flow rate is considered in the simulations.

The shapes and the sizes of each dome were selected to obtain eigenfrequencies, $f_{m,n,p}$ close to the frequency of the acoustic field forced in the main cavity, e.g., 1 kHz. Here m, n, and p indicate the number of nodes respectively in the direction $\vec{x}$, $\vec{y}$, and $\vec{z}$.

The *gas dome GD* (left side in Figure 3) presents a rectangular section and encloses a part of the three injector bodies. The link between an injector and the dome is ensured by two diametrically opposite holes drilled in the injector body. The diameter of these holes d_{or} can be changed by replacing the internal insert. The length L_{GD} and the height H_{GD} of the dome were fixed as simulations indicated that the width W_{GD} of the dome was the parameter that most strongly affected the resonant modes of interest. Thus, two pistons were placed on the vertical boundary surfaces in order to vary the dome size W_{GD}. The smallest gas dome volume will be indicated in the following as *GD*0 and the largest one as *GD*8.

The mode shapes GD-A, GD-B, and GD-C of the three *GD* eigenfrequencies closest to 1 kHz, predicted by the simulations, are reported in Figure 5 for $d_{or} = 1.125$. Characterization of numerical mode shapes is given as a function of the reduced coordinates: $\tilde{x}_g = x/W_{GD8}$ and $\tilde{y}_g = y/L_{GD}$. Figure 5(a) represents the real part of the complex pressure amplitude distribution calculated for *GD*0. The envelope profiles of the pressure amplitude of the acoustic waves along $\tilde{x}_g$ and $\tilde{y}_g$ are also reported in Figure 5(b) and (c). These profiles are calculated at the gas dome mid-height ($H_{GD}/2$) for $\tilde{y}_g = 0.16$ and $\tilde{x}_g = 0.11$ respectively (see Figure 5(a)). The influence of the dome size on the mode frequencies is indicated in Figure 6.

For mode GD-A, numerical acoustic pressure distributions indicate that, in the vertical planes $\tilde{y}_g = constant$, all points are in-phase (see Figure 5(a)) and acoustic pressure has a maximum at $\tilde{x}_g = 0$ and decreases toward the dome boundaries at $\tilde{x}_g = \pm 0.5$. The vertical symmetry plane $\tilde{y}_g = 0$ is the nodal plane, $f_{0,1,0}$ (see Figure 5(c)). Calculations indicate (Figure 6) that the eigenfrequency associated with mode GD-A increases from 950 to 1005 Hz by increasing the dome size.

Mode GD-B presents a spatial structure similar to GD-A along the $\tilde{x}_g$-axis (see Figure 5(b)). In every plane $\tilde{z}_g = constant$, two nodal lines parallel to $\tilde{x}_g$ are identified, $f_{0,2,0}$ (see Figure 5(c)). In both plots, curves corresponding to *GD*0, *GD*4, and *GD*8 are superimposed. Increasing the dome size does not affect the associated eigenfrequency, which varies between 1040 and 1050 Hz.

The third mode, named GD-C, changes its shape as the dome size is increased. For *GD*0, *GD*2, and *GD*4 all

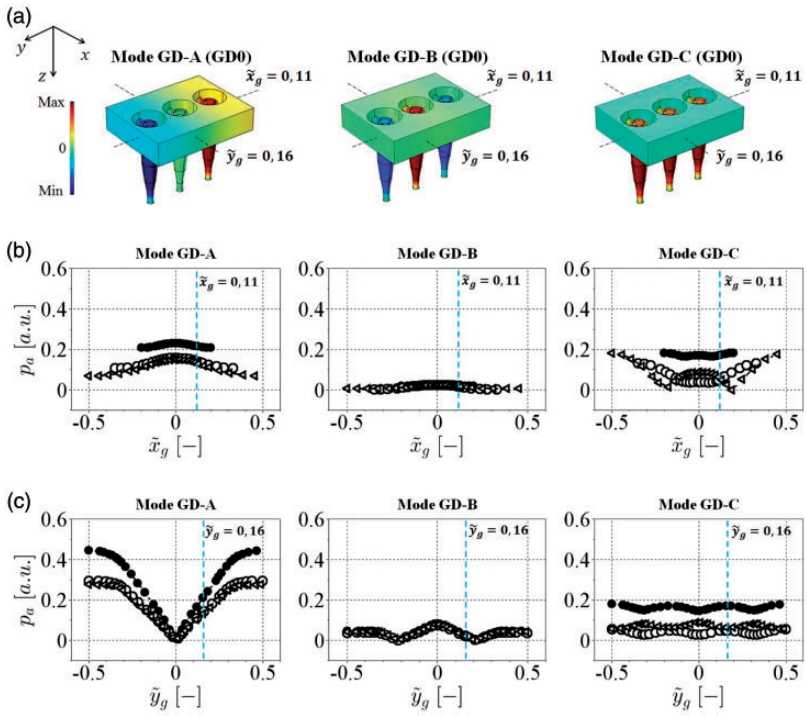

Figure 5. Gas dome mode-shapes obtained with COMSOL Multiphysics®: (a) real part of the complex pressure amplitude distribution for *GD*0 ($d_{or} = 1.125$); (b) envelope profiles of pressure amplitudes at $\tilde{y}_g = 0.16$ w.r.t. $\tilde{x}_g = x/W_{GD8}$; (c) envelope profiles of pressure amplitudes at $\tilde{x}_g = 0.11$ w.r.t. $\tilde{y}_g = y/L_{GD}$ (● = *GD*0; ○ = *GD*4; ◁ = *GD*8; $d_{or} = 1.125$).

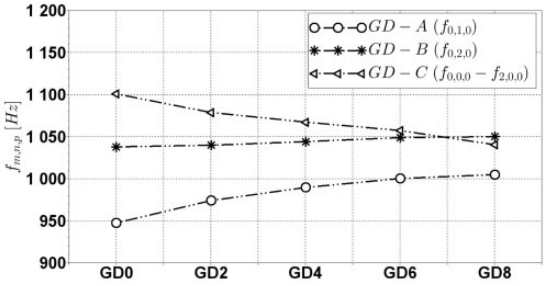

Figure 6. Gas dome eigenfrequencies as function of dome size ($d_{or} = 1.125$).

points in the dome cavity are in phase (see Figure 5(a)) and the dome acts as a Helmholtz resonator ($f_{0,0,0}$). For *GD*6 and *GD*8, two nodal lines appear in the $\tilde{y}_g$-direction ($f_{2,0,0}$). In the $\tilde{x}_g$-direction, acoustic pressure amplitudes at the pistons' walls are of the same order of magnitude as those observed for *GD*0. Increasing the dome size produces an associated eigenfrequency which decreases from 1100 Hz to roughly 1040 Hz. The frequency response of the three modes GD-A, GD-B, and GD-C (Figure 6) are in agreement with the experimental characterization of the dome frequency response reported in Appendix 1. Indeed, dome frequency response to a white noise excitation indicates that by increasing the dome size the eigenfrequencies of the dome get closer to the forcing frequency. In Figure 15, a narrowing of the effective spectrum is noted when the size increases from *GD*0 to *GD*8.

The *liquid dome LD* (right side in Figure 3) has a cylindrical geometry. The diameter of the dome d_{LD} is fixed in this analysis, while its length L_{LD} can be varied by means of two pistons. The smallest liquid dome volume is indicated in the following as *LD*0 and the largest as *LD*2. The dome is connected to the injectors by three connection junctions. The length L_j and the diameter d_j of the junctions are two adjustable parameters.

Figure 7 represents two eigenmodes predicted by the simulations. The real part of the complex pressure amplitude distributions are represented in Figure 7(a) while the envelope profiles of the pressure amplitude calculated along the liquid dome symmetry axis (see Figure 7(a): $\tilde{x}_g = \tilde{z}_g = 0$) are reported in Figure 7(b). Reduced coordinates considered for the liquid mode characterization are $\tilde{x}_l = x/d_{LD}$, $\tilde{y}_l = y/L_{LD}$, and $\tilde{z}_l = z/d_{LD}$. The corresponding eigenfrequencies are shown in Figure 8 as functions of the liquid dome size. The eigenfrequency associated to mode LD-A is around 1000 Hz for all dome sizes. If the eigenmode is excited all points in the whole domain are in-phase ($f_{0,0,0}$). Mode LD-B is reported here even though its

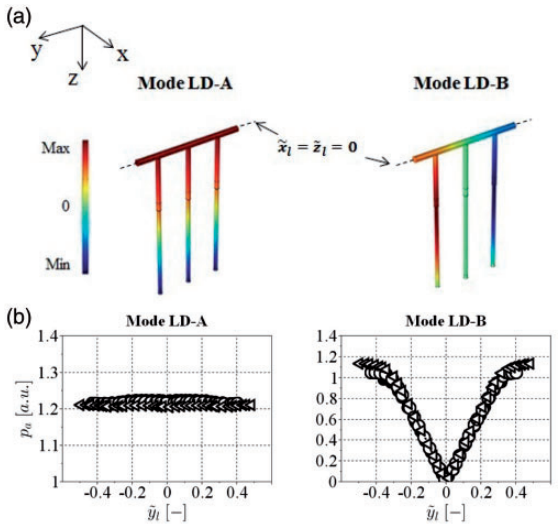

Figure 7. Liquid dome mode-shapes obtained with COMSOL Multiphysics®: (a) real part of the complex pressure amplitude distribution (*LD*1); (b) envelope profiles of pressure amplitudes w.r.t. $\tilde{y}_l = y/L_{LD}$ (● = *LD*0; ○ = *LD*1; ◁ = *LD*2; $L_j = 0.548$; $d_j = 0.67$).

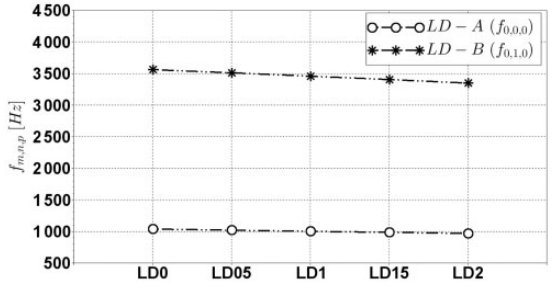

Figure 8. Liquid dome eigenfrequencies as a function of dome size ($L_j = 0.548$, $d_j = 0.67$).

corresponding eigenfrequency is around 3500 Hz, because its spatial structure indicates the presence of a pressure node at the central injector, whilst the extremities of the two domes oscillate out-of-phase.

4. Results and discussion

All tests have been performed by forcing the second transverse cavity mode at a frequency of 1 kHz and at the maximum available acoustic pressure level corresponding to a peak-to-peak amplitude of 12 kPa at PAN. Results indicate that both gas and liquid domes are sensitive to acoustic coupling.

4.1. Acoustic response of the gas dome

For all the tested configurations, results indicate that the response of the injection system is strongly affected by the acoustic conditions imposed at the injectors' outlets and by the design parameters. Figures 9 and 10 show the peak-to-peak acoustic pressure amplitudes measured with the pressure transducers inside the

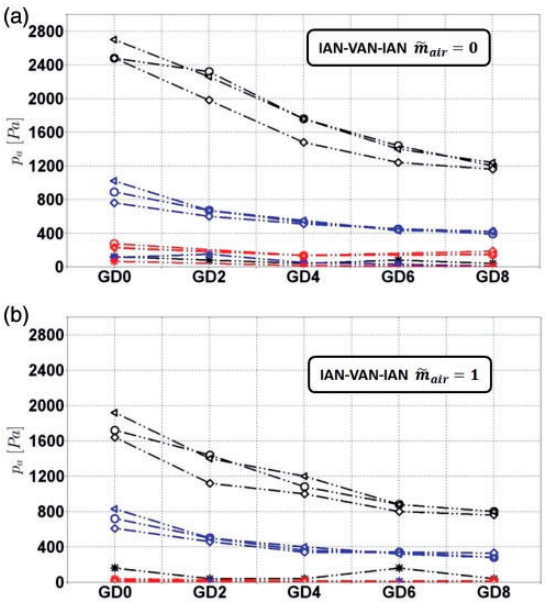

Figure 9. Peak-to-peak acoustic pressure measurements in the gas dome as a function of the dome size for the three connection diameters at: (a) IAN-VAN-IAN, $\tilde{m}_{air} = 0$ and (b) IAN-VAN-IAN, $\tilde{m}_{air} = 1$ (○ = PT_{l0}; * = PT_{c0}; ◇ = PT_r0; ◁ = PT_l1; red $d_{or} = 0.375$; blue $d_{or} = 0.75$; black $d_{or} = 1.125$).

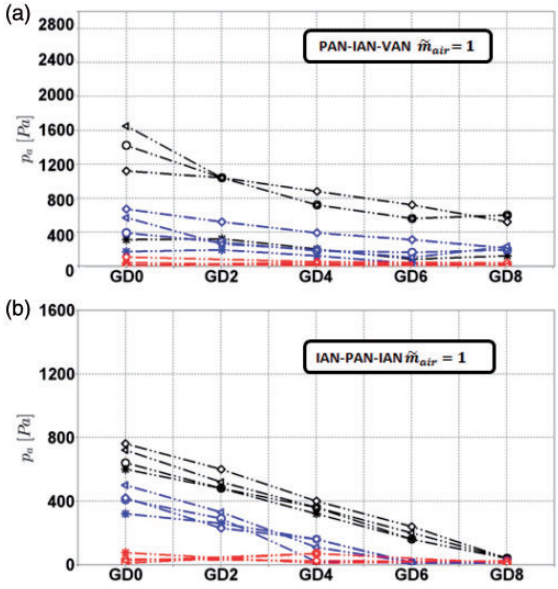

Figure 10. Peak-to-peak acoustic pressure measurements in the gas dome as a function of the dome size for the three connection diameters at: (a) PAN-IAN-VAN, $\tilde{m}_{air} = 1$ and (b) IAN-PAN-IAN, $\tilde{m}_{air} = 1$ (○ = PT_{l0}; * = PT_{c0}; ◇ PT_{r0}; ◁ PT_{l1}; red $d_{or} = 0.375$; blue $d_{or} = 0.75$; black $d_{or} = 1.125$).

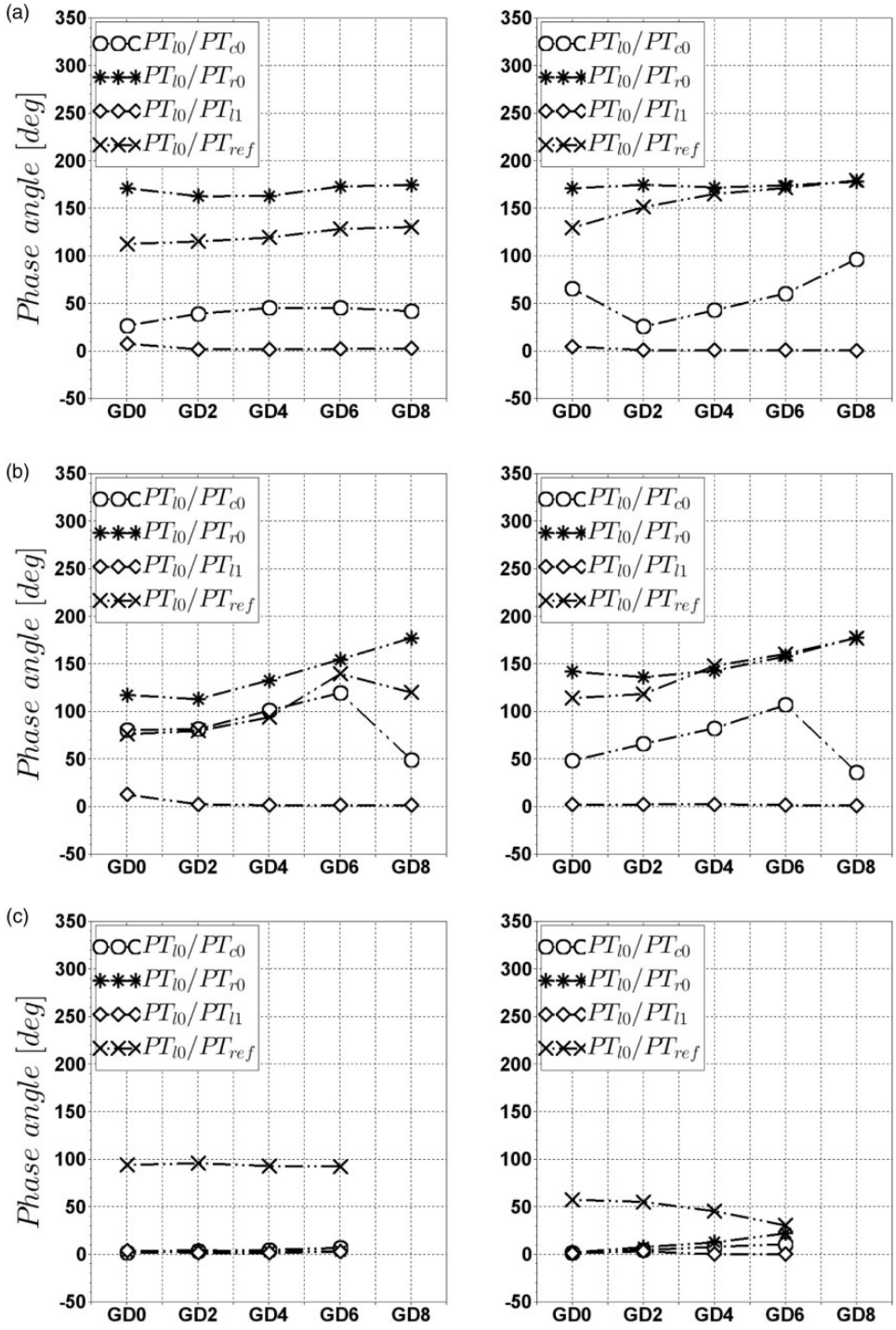

Figure 11. Experimental phase-shifts between the PT_{l0} signal and PT_{c0}, PT_{r0}, PT_{l1}, and PT_{ref} signals as functions of the dome size, for $d_{or} = 0.75$ (left side) and $d_{or} = 1.125$ (right side) at: (a) IAN-VAN-IAN, (b) PAN-IAN-VAN, and (c) IAN-PAN-IAN.

dome, while Figure 11 summarizes the pressure transducers' phase-shifts.

In all the configurations, the acoustic level measured in the gas dome decreases as its size is increased. Indeed, a crucial decrease in energy density associated with the eigenmodes is observed in data reported in Figure 15 in Appendix 1. A decrease of the acoustic pressure amplitude in the gas dome is also observed by increasing the mass flow rate due to an increase in the pressure drop. Similarly, decreasing the orifice diameter d_{or} also induces an increase in the pressure drop and a lower response.

The IAN-VAN-IAN configuration indicates the strongest acoustic response. The maximum acoustic pressure fluctuation in the domes is 2800 Pa, i.e., 23% of the acoustic pressure level measured at PAN in the main cavity. This fluctuation is measured without any flow rate while for the maximum flow rate considered here, ($\tilde{m}_{air} = 1$) the acoustic pressure fluctuation amplitude reaches only 2000 Pa, i.e., 17% of the acoustic level at PAN in the main cavity. The three pressure transducer signals PT_{l0}, PT_{r0}, and PT_{l1} have the same acoustic pressure fluctuation amplitudes. Moreover, PT_{c0} shows a quasi null signal (see Figure 9). Pressure fluctuations of PT_{l0} and PT_{l1} are in-phase while of PT_{l0} and PT_{r0} are always out-of-phase irrespective of the dome size. All these features are in accordance with the eigenmode GD-A of the gas dome presented in Figure 5: all points in vertical planes $\tilde{y}_g = constant$ are in-phase (see Figure 5(a) and (b)) and $\tilde{y}_g = 0$ is a nodal plane (see Figure 5(c)). Pressure transducers PT_{l2} and PT_{l3} provide complementary information on the acoustic pressure distribution inside the dome. As shown in the study of Ficuciello,[27] these measurements show a global trend of decrease of the pressure amplitude along $\tilde{x}_g$. This is also consistent with mode GD-A (Figure 5(a)) where coordinates $\tilde{x}_g = 0.17$, $\tilde{x}_g = 0.32$, and $\tilde{x}_g = 0.47$ correspond to the locations of PT_{l1}, PT_{l2}, and PT_{l3}, respectively. Finally Figure 9 indicates that for $\tilde{x}_g = \pm 0.17$, pressure amplitude decreases when dome size is increased. In combination with the identification of mode GD-A, this indicates that a decrease of the pressure amplitude is likely to occur in the whole dome.

A decrease of the acoustic pressure amplitude in the gas dome is also observed by decreasing the orifice diameter d_{or}. The influence of the size of d_{or}, on the acoustic coupling between the gas dome and the main cavity, can also be noticed in the phase-shift between the signal of PT_{l0} and the signals of PT_{c0}, PT_{r0}, PT_{l1}, and PT_{ref}, which are reported in Figure 11 (PT_{ref} is the signal of the transducer placed in the main cavity at PAN). With $d_{or} = 1.125$, acoustic coupling is facilitated and the phase-shift between PT_{l0} and PT_{ref} varies continuously with the dome size. Since the change in the dome size modifies the internal mode shapes, the phase-shift between two spatially fixed points is affected. The phase-shift inside the gas dome, i.e., between PT_{l0} and PT_{c0}, also varies from 45° to 90°, due to the modification of the dome's internal mode shapes. The phase difference between VAN and IAN is expected to be different from zero. Indeed, it was shown by Cáceres et al.[28] that in the vicinity of a VAN of such a transverse acoustic field phase-shift varied continuously from 0 to + π. Thus, in our case, the phase difference between VAN and IAN is expected to be different from zero.

On the contrary, with $d_{or} = 0.75$, the phase-shifts are independent of the dome size. Indeed, the boundary condition near the orifice is not far from that given by the wall condition; thus, measurement at PT_{l0} does not vary with the size of the gas dome. Thus, the mode shapes established in each cavity are not dependent on each other and the phase-shift between PT_{l0} and PT_{ref} remains fixed, as well as the phase-shift between PT_{l0} and PT_{c0} which is always 50°.

At PAN-IAN-VAN, the maximum acoustic response of the injection system is 1600 Pa. In this configuration, the dome is submitted to the largest pressure fluctuation range, due to the presence of both pressure and VANs, at the injectors' exits (see Figure 2). As explained before, for the IAN-VAN-IAN configuration in the vicinity of the VAN, phase-shift is expected to vary continuously from 0 to $+\pi$. Measurements are thus very sensitive to the position of the pressure transducers, which causes the phase-shifts of PT_{l0} with PT_{c0}, PT_{r0} and PT_{ref} to vary with the dome size for both $d_{or} = 0.75$ and $d_{or} = 1.125$ (see Figure 11(b)). The acoustic pressure fluctuations inside the dome decrease when the dome's size is increased, which is in agreement with calculations as shown in Figure 5.

At IAN-PAN-IAN, the maximum acoustic response of the injection system is 800 Pa. This configuration is centered in the cavity. The three injectors are submitted to in-phase acoustic pressure fluctuations, with amplitudes larger than those of the two previous cases. The acoustic condition imposed in this case facilitates the establishment of the GD-C mode (see Figure 5 mode GD-C). This is confirmed experimentally by in-phase (see Figure 11(c)) and same-amplitude (see Figure 10) pressure signals in the dome. As observed earlier, the gas dome is more likely to respond to acoustic excitation for larger junction diameters. For $d_{or} = 0.75$, phase-shifts are independent of the dome size, while for $d_{or} = 1.125$, they change slightly as dome size is

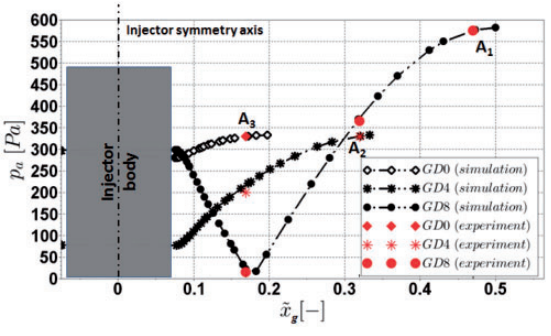

Figure 12. Acoustic pressure amplitude with acoustic coupling in the cavity along the gas dome width. Numerical results are compared to experimental measurements (each curve is scaled by the maximum value A_i, with $i \in (1,3)$).

increased. This slight change is due to the fact that the mode shape changes in this case. Indeed, simulations indicate that when dome size is increased, the eigenmode changes its mode shape (see Figure 5 mode GD-C). A good agreement between pressure amplitudes measured by PT_{l1}, PT_{l2}, and PT_{l3} and those predicted by simulations is shown in Figure 12. In this case, simulations take into account the main cavity and the gas dome simultaneously. The Helmholtz equation is solved with boundary conditions at the loudspeakers corresponding to a given normal harmonic acceleration fluctuating at the forcing frequency. Numerical curves are scaled by the maximum experimental value, indicated as A_i in the figure.

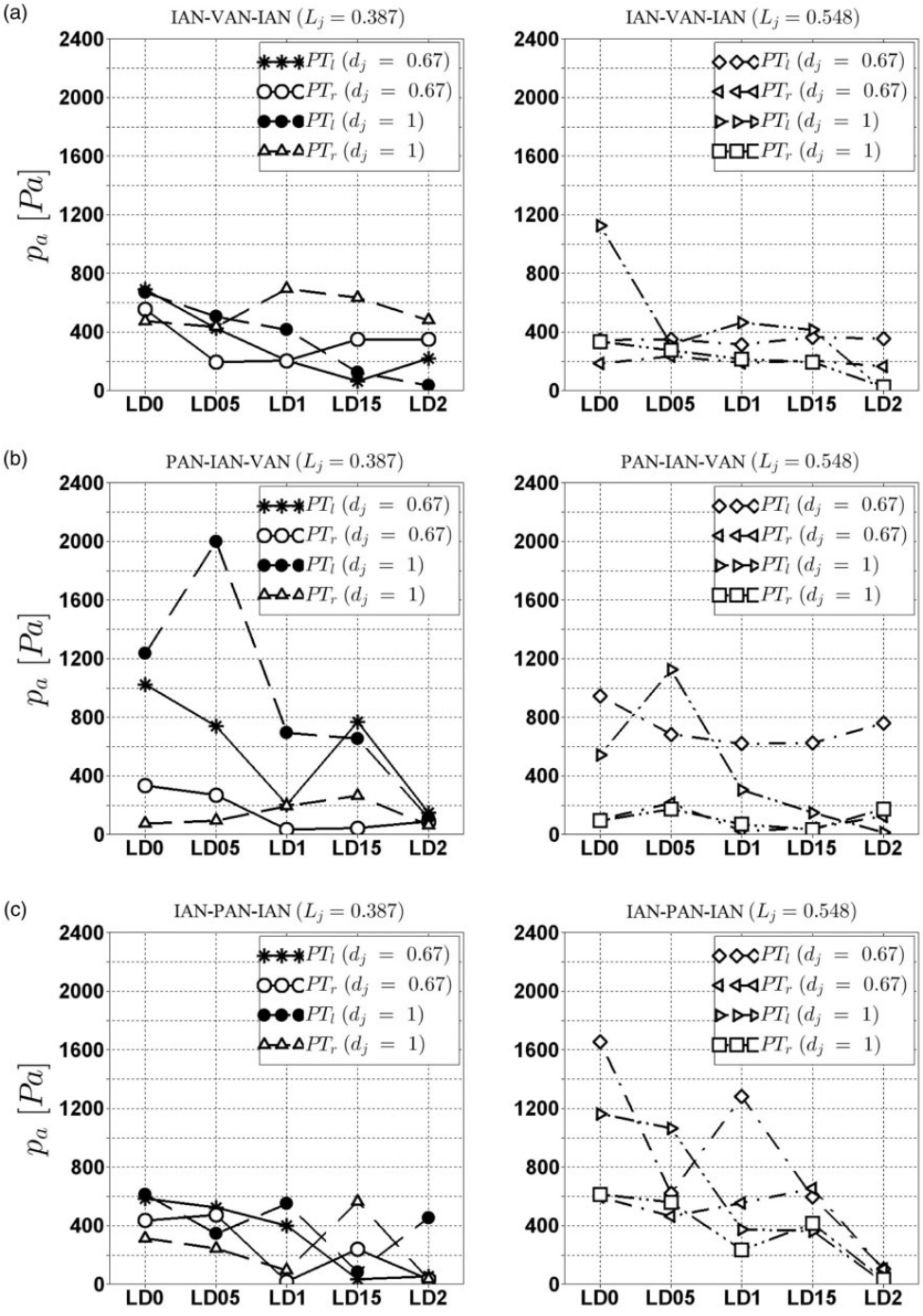

Figure 13. Acoustic response of the liquid dome as a function of the dome size for the three connection lengths at: (a) IAN-VAN-IAN, (b) PAN-IAN-VAN, and (c) IAN-PAN-IAN.

The appearance of the nodal line is clearly visible at $GD8$. Increasing the dome size at IAN-PAN-IAN does not induce a decrease of acoustic pressure fluctuation amplitudes in all points, as it does in the other two configurations. Indeed, pressure amplitude measured with PT_{l3} at $GD8$ is higher than the one measured by PT_{l0} at $GD0$, due to the mode-shape veering. Acoustic pressure amplitudes detected in the dome are always lower than 800 Pa, which corresponds to 6.7% of the acoustic pressure amplitude imposed in the main cavity at PAN. However, even when the cavity acoustic pressure amplitudes are maximum at IAN-PAN-IAN, the response of the dome in this configuration is always lower than in the other two cases. The fact that the maximum acoustic response in the dome does not correspond to the maximum acoustic pressure fluctuations in the cavity indicates that the dome acoustics has an important role in the acoustic interaction between the injection system and the main cavity.

The acoustic response of the gas dome strongly depends on the considered parameters and the dependence on such parameters has a unique tendency. For all configurations, the acoustic coupling between the dome and the main cavity is weakened by increasing the mass flow rate and the dome size and by decreasing the connection diameters. The only exception is represented by IAN-PAN-IAN. In this latter configuration, acoustic pressure amplitudes measured in the dome decrease with the dome size until $GD6$; for a further increment of the dome size, the acoustic pressure amplitudes measured in the gas dome increase. By changing the position of the dome with respect to the acoustic axis, different excitation conditions are imposed on the injection system and consequently different mode shapes are excited inside the injection dome. Mode shapes observed experimentally are in agreement with the numerical simulations.

4.2. Acoustic response of the liquid dome

Figure 13 shows the amplitudes recorded by PT_l and PT_r (schematic representation in Figure 4), while Figure 14 shows the phase-shift between their signals. Both quantities are expressed as functions of the dome size, L_j and d_j for the three spatial configurations considered (IAN-VAN-IAN, PAN-IAN-VAN, and IAN-PAN-IAN).

For the IAN-VAN-IAN configuration, the liquid dome's acoustic pressure amplitudes (Figure 13(a)) are always lower than 1200 Pa (10% of the maximum acoustic pressure in the main cavity). Changing the junction diameter or length, or the dome size the liquid dome response, does not present a uniform trend. But for $L_j = 0.387$, the acoustic pressure

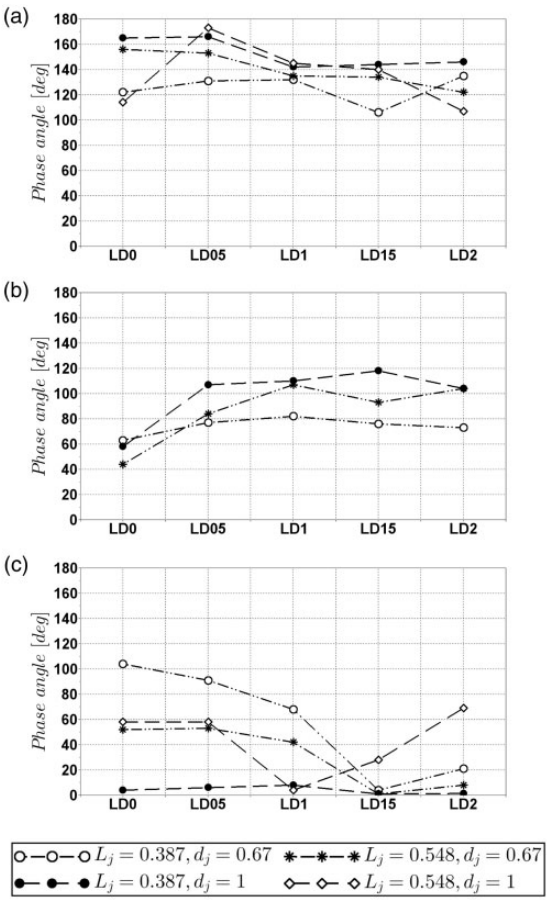

Figure 14. Experimental phase-shift between the PT_l and PT_r signals as a function of the dome size and L_j at: (a) IAN-VAN-IAN, (b) PAN-IAN-VAN, and (c) IAN-PAN-IAN.

measurement of PT_l continuously decreases with increasing dome size, especially for $d_j = 1$. As shown in Figure 14(a), the acoustic pressure signals measured with PT_l and PT_r tend to be out-of-phase. The phase-shift between transducers suggests a spatial distribution of the acoustic pressure similar to that of the LD-B mode shape (see Figure 7). However, the power spectral density does not present any content around 3500 Hz.

In the PAN-IAN-VAN configuration, the response is more sensitive to the dome size and the acoustic pressure amplitudes decrease with the dome size (see Figure 13(b)). A peak is measured for $LD05$: it equals 2000 Pa for the shortest junction length and diminishes to 1200 Pa for the longest one. The phase-shift between the transducers ranges between 40° and 120°, as shown in Figure 14(a), which does not correspond to that of the simple eigenmodes calculated and presented in Figure 5.

For the IAN-PAN-IAN configuration and for $L_j = 0.387$, acoustic pressure amplitudes (Figure 13(c)) are the lowest and do not exceed 700 Pa. For $L_j = 0.548$, a stronger response of the liquid dome is obtained.

For $d_j = 0.67$, two peaks are observed for $LD0$ and $LD1$, 1600 Pa and 1250 Pa, respectively. In Figure 14(c), the phase-shift between left and right transducers indicates that signals are perfectly in-phase for $d_j = 1$ and $L_j = 0.387$, in agreement with the onset of the mode LD-A (see Figure 7, mode LD-A). For $d_j = 1$ and $L_j = 0.548$, the response is more complex. For $d_j = 0.67$, the pressure transducers phase-shift decreases from 100° to 0° for $L_j = 0.387$ and from 60° to 0° for $L_j = 0.548$.

Results indicate that in some conditions, the liquid dome can present acoustic pressure fluctuations of the same order of magnitude as that observed in the gas dome. The general tendency is to reduce the acoustic response by increasing the dome size. However, results indicate that the liquid dome's acoustic response is more complex than that of the gas dome since amplitude fluctuations are not affected in a unique manner by the investigation parameters.

5. Conclusion

The acoustic interaction between a high-amplitude transverse acoustic field and an injection system has been investigated. A wide-ranging parametric analysis has been performed and the response of the system has been tested in several configurations. The objective of this investigation was to observe how an injection system could respond to the acoustic pressure fluctuations coming from an instability established in a combustion chamber.

Two injection domes, one for the gas and one for the liquid, have been expressly designed in order to investigate the acoustic coupling at the forcing frequency of 1 kHz. The two domes were used to feed three coaxial injectors similar to those used in liquid rocket engine applications.

By changing the position along the acoustic axis, different excitation conditions are imposed on the injection system and thus different mode shapes are excited inside the injection domes. In most of the cases, eigenmode simulations allow the mode shapes excited experimentally to be identified. However in some cases, the response of the domes, particularly of the liquid dome, is more complex and direct identification is not possible.

The response of the injection system is strongly affected by the acoustic boundary conditions at injector outlets and by all the geometrical parameters considered here. In all the configurations, the acoustic coupling between the gas dome and the main cavity is weakened by increasing the mass flow rate and the dome size, and by decreasing the diameter of the orifices between the injectors and the gas dome. The only exception is represented by the IAN-PAN-IAN configuration, in which an excessive increase of the dome size causes an increase of the acoustic response due to a shape modification of the exited mode (see Figure 12). For the IAN-VAN-IAN configuration, the boundary conditions imposed at the injector's exit plane, in terms of acoustic pressure amplitudes in the main cavity, are lower than those corresponding to PAN-IAN-VAN and IAN-PAN-IAN configurations. But, the gas dome shows the strongest acoustic response for this configuration. This indicates that the dome acoustics plays a role in the acoustic coupling mechanism between the main cavity and the injection system.

Concerning the liquid dome response, the general tendency is to discourage the acoustic coupling by increasing the dome's size. The liquid dome's response does not seem to be strongly sensitive to the parameters studied here for the IAN-VAN-IAN configuration except for the acoustic pressure measurement of PT_l with $L_j = 0.387$ which continuously decreases with increasing dome size. But, the liquid dome shows a strong acoustic response in some conditions for PAN-IAN-VAN and IAN-PAN-IAN configurations.

The main conclusion is that both liquid and gas domes show a strong response to the transverse acoustic field established in the main cavity. The maximum of acoustic pressure fluctuation amplitudes attains 23% of the amplitudes of the acoustic pressure forced in the main cavity (without mass flow rate). In an actual propulsion system, such a high level of fluctuations in the injection dome could induce strong mass flow-rate fluctuations. In fact, mass flow-rate fluctuations can contribute significantly to the acoustic fluctuation amplification in the combustion chamber.

Moreover, the maximum response of the domes is not observed in the configuration where the injection system is submitted to the highest acoustic pressure fluctuations of the cavity (IAN-PAN-IAN configuration), but rather where the phase-shift conditions can excite a particular dome eigenmode, as in the IAN-VAN-IAN configuration for the gas dome.

Domes' geometries considered here do not replicate actual rocket engine geometries. However, results presented in this study open the path to the definition of general rules that could be used early in design phases, together with numerical simulations, to anticipate and justify the acoustic coupling behavior of domes/main combustion device cavity and represent a starting point for future investigation.

Declaration of Conflicting Interests

The author(s) declared no potential conflicts of interest with respect to the research, authorship, and/or publication of this article.

Funding

The author(s) disclosed receipt of the following financial support for the research, authorship, and/or publication of this article: This research is funded by the CNES R&D program, in the framework of the activity of the French-German research group REST (Rocket Engine Stability Research Initiative).

References

1. Yang V and Anderson W. *Liquid rocket engine combustion instability*. Progress in Astronautics and Aeronautics. Vol. 169. Washington, DC: AIAA, 1995.
2. Harrje D and Reardon F. *Liquid propellant rocket combustion instability*. Technical Report, NASA-SP-194, 1972. Washington, DC: NASA.
3. Oefelien J and Yang V. Comprehensive review of liquid-propellant combustion instabilities in f-1 engines. *J Propul Power* 1993; 9: 657–677.
4. Fisher S, Dodd F and Jensen R. Scaling techniques for liquid rocket combustion stability testing. In: Yang V and Anderson W (eds) *Liquid rocket engine combustion instability*. Progress in Astronautics and Aeronautics. Vol. 169. Washington, DC: AIAA, 1995, pp. 545–564.
5. Culick FEC. *Combustion instabilities in liquid-fueled propulsion systems – an overview*, AGARD 72B PEP Meeting, 1988.
6. Hutt J and Rocker M. High-frequency injection-coupled combustion instability. In: Yang V and Anderson W (eds) *Liquid rocket engine combustion instability*. Progress in Astronautics and Aeronautics. Vol. 169. Washington, DC: AIAA, 1995, pp. 345–555.
7. Sirignano WA, Delplanque JP, Chiang CH, et al. Liquid-propellant droplet vaporization: A rate-controlling process for combustion instability. In: Yang V and Anderson W (eds) *Liquid rocket engine combustion instability*. Progress in Astronautics and Aeronautics. Vol. 169. AIAA, Washington, DC: AIAA, 1995, pp. 307–343.
8. Chehroudi B. Physical hypothesis for the combustion instability in cryogenic liquid rocket engines. *J Propul Power* 2010; 26(6): 1153–1160.
9. Hardi J, Oschwald M and Dally B. Flame response to acoustic excitation in a rectangular rocket combustor with lox/h2 propellants. *CEAS Space J* 2011; 2: 41–49.
10. Méry Y. *Mécanismes d'instabilités de combustion haute-fréquence et application aux moteurs-fusées*. PhD Thesis, École Centrale Paris, EM2C, France, 2010.
11. Hakim L. *Dynamics of transcritical coaxial flames in high-frequency transverse fields: application to liquid rocket engine instabilities*. PhD Thesis, École Centrale Paris, EM2C, France, 2013.
12. Chehroudi B and Talley D. Preliminary visualizations of acoustic waves interacting with subcritical and supercritical cryogenic jets. In: *15th annual conference on liquid atomization and spray systems (ILASS Americas)*, 14–17 May 2002, Madison, WI.
13. Vingert L, Gicquel P and Lourme D. Coaxial injector atomization. In: *Liquid rocket engine combustion instability*. Progress in Astronautics and Aeronautics. Vol. 169. AIAA, 1995, pp. 145–189.
14. Heidmann M and Groeneweg J. *Analysis of the dynamic response of liquid jet atomization to acoustic oscillations*. NASA TN D-5339, 1969. Cleveland, OH: NASA Lewis Research Center.
15. Oschwald M, Farago Z, Searby G, et al. Resonance frequencies and damping of a combustor acoustically coupled to an absorber. *J Propul Power* 2008; 24: 524–533.
16. Sliphorst M, Gröning S and Oschwald M. Theoretical and experimental identification of acoustic spinning mode in a cylindrical combustor. *J Propul Power* 2011; 27: 182–189.
17. Gröning S, Hardi J, Suslov D, et al. Injector-driven combustion instabilities in a hydrogen/oxygen rocket combustor. *J Propul Power* 2016; 32: 560–573.
18. Searby G, Nicole A, Habiballah M, et al. Prediction of the efficiency of acoustic damping cavities. *J Propul Power* 2008; 24: 516–523.
19. Hardi J, Oschwald M and Dally B. Acoustic characterisation of a rectangular rocket combustor with lox/h2 propellants. In: *4th European conference for aerospace sciences*, 4–8 July 2011, St. Petersburg, Russia.
20. Hardi J. *Experimental investigation of high frequency combustion instability in cryogenic oxygen-hydrogen rocket engines*. PhD Thesis, School of Mechanical Engineering of Adelaide, Australia, 2012.
21. Hardi J, Beinke S, Oschwald M, et al. Coupling behaviour of lox/h2 flames to longitudinal and transverse acoustic instabilities. In: *48th AIAA/ASME/SAE/ASEE joint propulsion conference & exhibit*, Atlanta, Georgia, 30 July – 1 August 2012. AIAA.
22. Urbano A, Selle L, Staffelbach G, et al. Exploration of combustion instability triggering using large eddy simulation of a multiple injector liquid rocket engine. *Combust Flame* 2016; 169: 129–140.
23. Baillot F, Blaisot JB, Boisdron G, et al. Behavior of an air-assisted jet submitted to a transverse high frequency acoustic field. *J Fluid Mech* 2009; 640: 307–344.
24. Ficuciello A, Blaisot JB, Baillot F, et al. Response of coaxial air-assisted liquid jets in an acoustic field: atomization and droplets clustering. In: *13th international conference on liquid atomization and spray system (ICLASS)*, 23–27 August 2015, Tainan, Taiwan.
25. Ficuciello A, Blaisot JB, Baillot F, et al. High amplitude acoustic field effects on air-assisted liquid jets. In: *52nd AIAA/SAE/ASEE Joint Propulsion Conference, AIAA Propulsion and Energy Forum*, 2016, paper no. 2016-5085, AIAA. doi:10.2514/6.2016-5085.
26. Ficuciello A, Blaisot JB, Richard C, et al. Investigation of air-assisted sprays submitted to high frequency transverse acoustic fields: droplet clustering. *Phys Fluid* 2017; 29: 067103. doi:10.1063/1.4985202.
27. Ficuciello A. *Analysis of high frequency/high amplitude acoustic field effects on coaxial injection: application to liquid rocket engine*. PhD Thesis, Normandie Université, Université de Rouen Normandie, France, 2017.
28. Cáceres M, Baillot F, Domingues E, et al. New experimental setup for thermoacoustic instabilities investigation in two-phase flow swirled combustion. In: *Proceedings of*

the 8th European combustion meeting (EMC), 18–21 April 2017, Dubrovnik, Croatia.
29. Faragó Z and Oschwald M. Resonance frequencies and damping in combustion chambers with quarter wave cavities. In: *6th symposium on launcher technologies*, 8–11 November 2005, Munich, Germany.

Appendix 1. Gas dome frequency response

The frequency response of the gas dome was investigated experimentally with a procedure similar to that found in the literature for the acoustic characterization of combustion chambers with quarter wave cavities.[29] A white noise signal was used to excite the dome. Dome size was varied from *GD*0 to *GD*8 and acoustic pressure was measured with the PT_{l1} pressure transducer (see Figure 4). The signal spectrum was then calculated and filtered in between 900 and 1200 Hz in order to focus on the spectrum region around 1000 Hz. Results are shown in Figure 15 for *GD*0 and *GD*8.

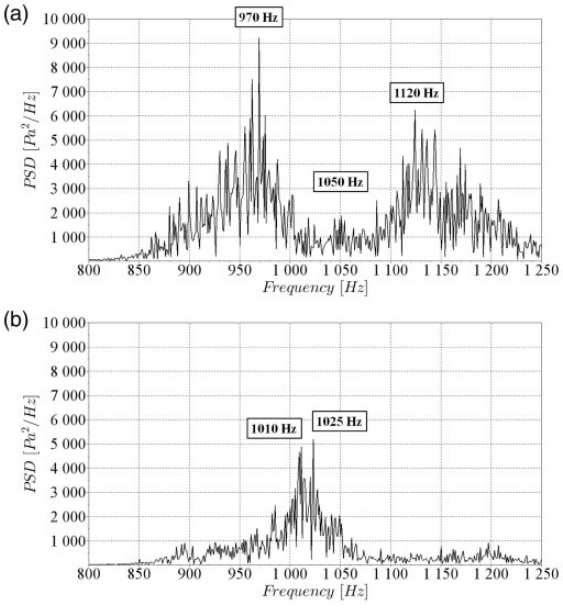

Figure 15. Experimental gas dome frequency response at white noise excitation for: (a) *GD*0 and (b) *GD*8 ($d_{or} = 1.125$).

By taking into account numerical results reported in Figure 6, the three modes GD-A, GD-B, and GD-C can be identified in the experimental spectrum of Figure 15(a) at 970 Hz, 1050 Hz, and 1120 Hz, respectively. Mode GD-B has very low energy compared with GD-A and GD-C, which is in agreement with Figure 5. For *GD*8 (see Figure 15(b)) the frequencies corresponding to GD-A and GD-C are closer than for *GD*0. This narrowing of the spectrum is in agreement with numerical results reported in Figure 6, in which eigenfrequencies get closer as gas dome size is increased. Moreover, by increasing the dome size, the density energy around 1000 Hz globally decreases, which explains why gas dome acoustic response decreases by increasing the dome size.